Supporting Information

Synthesis and transport properties of $[Ni_3Sn][Ni_{4-x}S_2]$, a *n*-type metal-rich sulfide with an intergrowth structure

Laura Agnarelli,*[a] Denis Pelloquin [a], Antoine Maignan [a] and Sylvie Hébert [a]

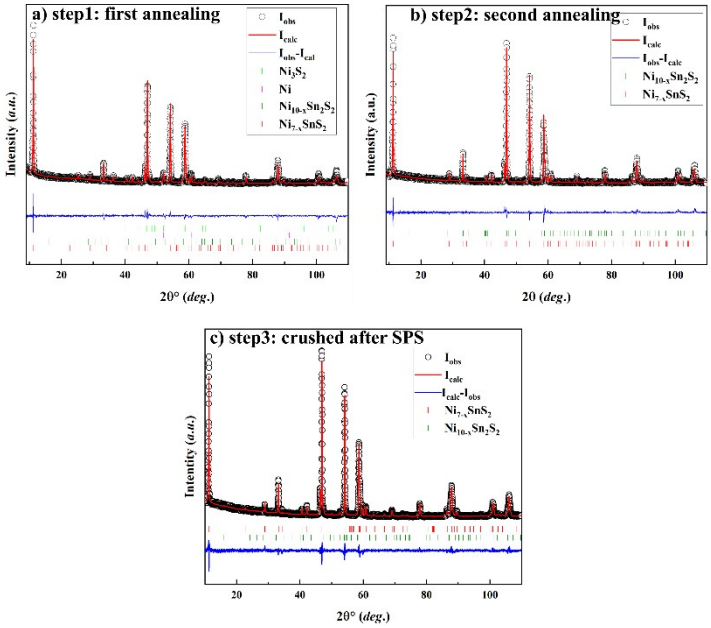

Fig. 1S. Rietveld refinement of the X-ray diffraction patterns of the sample with nominal composition Ni_6SnS_2 at different stages of the synthesis. Step 1 (a, after the first annealing): the refined phase composition is 78.5 wt% Ni_6SnS_2, 10.0 wt% $Ni_9Sn_2S_2$, 4.4 wt% Ni metal, and 7.25 wt% Ni_3S_2. Step 2 (b, after cold pressing into a pellet and second annealing): the refined phase composition is 98.5 wt% $Ni_6SnS_2$and 1.5 wt% $Ni_9Sn_2S_2$. Step 3 (after spark plasma sintering, SPS): the refined phase composition is 97.5 wt% $Ni_6SnS_2$and 2.5 wt% $Ni_9Sn_2S_2$. X-ray diffraction data were collected using Co $K\alpha_{1,2}$ radiation.

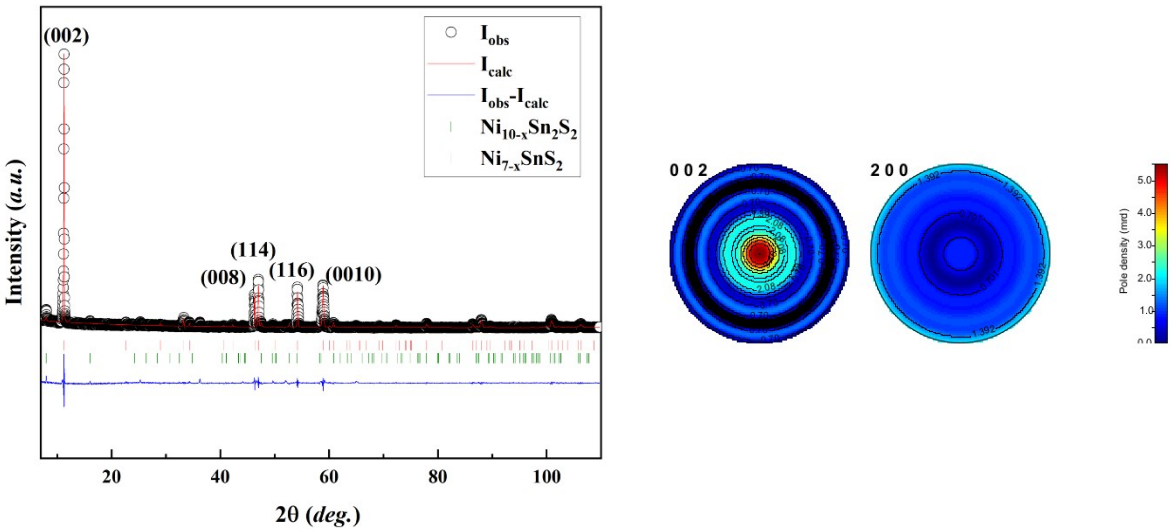

Fig. 2S. (left) Rietveld refinement of the X-ray diffraction pattern collected from the surface of the SPS pellet with nominal composition Ni_6SnS_2, revealing strong texturation with the crystallite *c*-axes preferentially oriented perpendicular to the pellet surface (i.e., parallel to the uniaxial pressure applied during SPS). X-ray diffraction data were collected using Co $K\alpha_{1,2}$ radiation. (right) Reconstructed pole figure derived from the spherical harmonics model used in the refinement, indicating a high density of crystallites with their *c*-axes aligned along the diffraction vector.

Table 1S. Crystallographic data for $Ni_{7-\delta}SnS_2$ from XRPD refinement after SPS treatment.

Composition	$Ni_{6.34}SnS_2$
Space group	*I*4/*mmm* (no. 139)
Lattice parameters	*a* = 3.6534(1) Å *c* = 18.170(2) Å *V* = 242.521(4) Å^3
Radiation, wavelength	Co radiation (λ_1 = 1.78897 Å, λ_2 = 1.79285 Å)
Profile fitting	Pseudo-Voigt [a]
χ^2	1.60

[a] Rietveld method

Table 2S. Atomic coordinates and isotropic displacement parameters for $Ni_{7-\delta}SnS_2$ determined from XRPD Rietveld refinement.

Atom	**site**	**Occupancy**	***x/a***	***y/b***	***z/c***	**B_{iso}**
Sn	2*a*		0	0	0	0.3623(1)
Ni1	8*g*		0	0.5	0.1064(1)	0.7596(1)
Ni2	2*b*		0.5	0.5	0	0.1131(1)
Ni3	4*e*	0.3690(1)	0	0	0.2114(1)	0.5645(1)*

Ni4	4*d*	0.3041(1)	0	0.5	0.25	0.5645(1)*
S	4*e*		0.5	0.5	0.1843(1)	0.3686(1)

* B_{iso} fixed for the refinement

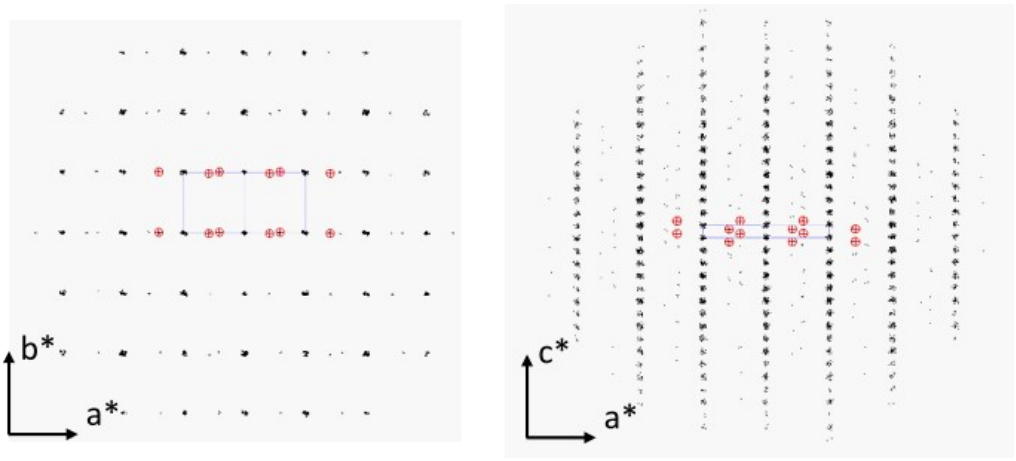

Fig. 3S. Electron diffraction patterns along [001] and [010] directions, revealing weak satellite reflections indicative of potential structural modulation.

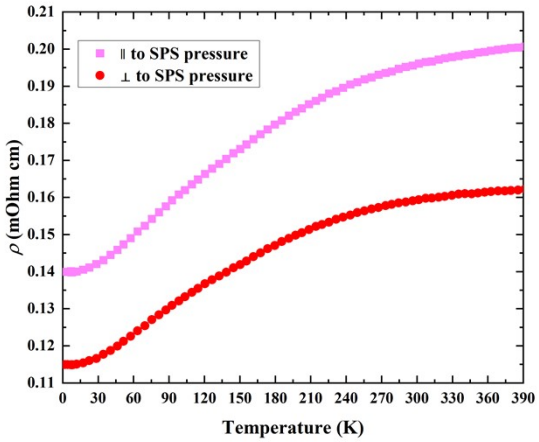

Fig. 4S. Temperature-dependent electrical resistivity (ρ) of Ni_6SnS_2 measured parallel to the SPS pressing direction (pink curve) and perpendicular to it (red curve). The data reveal significant resistivity anisotropy.

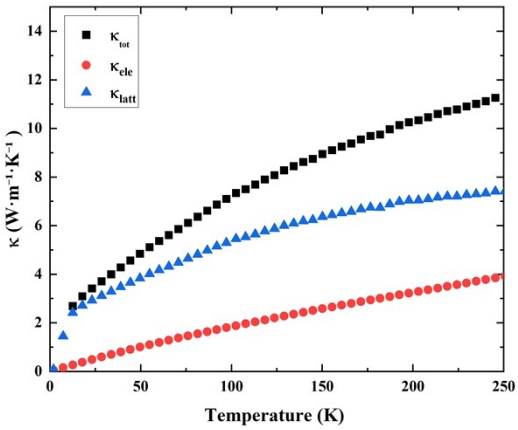

Fig. 5S. Temperature dependence of the total thermal conductivity (κ_{tot}, black squares), electronic thermal conductivity (κ_{ele}, red circles) and lattice thermal conductivity (κ_{latt}, blue triangles) of Ni_6SnS_2 measured from 250 K to 2 K along the direction perpendicular to the SPS pressing axis. The electronic contribution was estimated using the Wiedemann–Franz law with a Lorenz number $L = 2.44 \times 10^{-8}$ $W\Omega K^{-2}$.

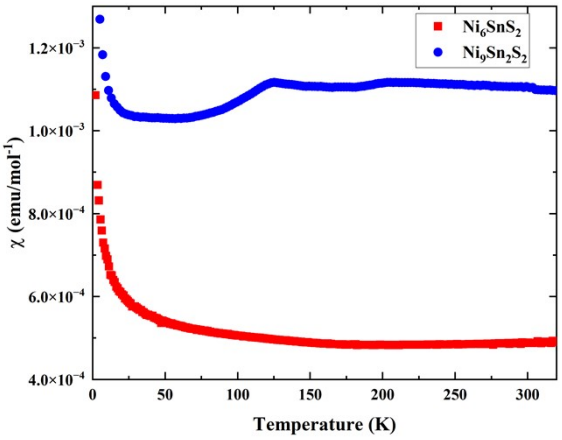

Fig. 6S. T dependence of magnetic susceptibility (χ) for Ni_6SnS_2 (red) and $Ni_9Sn_2S_2$ (blue) [12]. The data correspond to the zero-field-cooling measurements in 0.1T.